

Testing and evaluation of the structural performance of a 3D-printed polylactic acid aircraft wing rib

Ramona Dogea¹ · Xiu T. Yan¹ · Richard Millar²

Received: 30 March 2023 / Accepted: 4 May 2023

Published online: 10 May 2023

© Crown 2023 [OPEN](#)

Abstract

This paper presents an investigation of the structural performance of a 3D-printed Polylactic Acid (PLA) wing rib structure that is integrated with Internet of Things (IoT) sensory capabilities for application in an Industry 4.0 ecosystem. Both finite element analysis and experimental testing were employed to assess the strain distribution in the structure under various loading conditions and testing setups. The Taguchi approach was utilized to identify the physical factors and their interactions that have a significant impact on the strain distribution in the structure. The findings indicate that the bending load versus strain curve is highly influenced by the applied load position and wing rib cut-out locations, while the structural performance is also highly dependent on torsion. The incorporation of sensory locations with covers improved the component's ability to withstand traction load and resulted in a 61% reduction in corresponding strain. The most significant factor during bending tests was identified as the applied load, along with the interactions between the load location and crosshead speed of the testing machine.

Keywords Additive manufacturing · Aircraft wing rib · PLA material · Taguchi approach

1 Introduction

Additive manufacturing (AM) techniques have gained attention in both industrial and academic fields due to their flexibility in the choice of materials, rapid prototyping opportunities and capabilities for building parts with complex shapes. The Fused Deposition Modelling (FDM) technique, also known as Fusion Filament Fabrication (FFF), adds polymeric materials layer-by-layer to form a completed part. The material addition is coordinated by computer-aided design (CAD) software, that communicates to the printer where the polymer should be added [1]. In FDM a filament is drawn through a heating extrusion head, which adds the molten material onto the bed where the 3D part is built [2]. The quantitative and qualitative impacts of the 3D printing process are being investigated by researchers who have determined that the quality of 3D printed parts vary depending on the shape, material, and specific 3D printer used. The Fused Filament Fabrication (FFF) 3D printing method often produces unsatisfactory results due to various parameters that can affect the print quality and waste time, energy, and materials. To prevent such issues, suitable parameter values must be selected, based on the user's expertise and experience [3]. Most parameters are determined using software provided by FFF printer manufacturers. Skilled users commonly share software templates to help new users achieve better results. Relevant research studies and instructions from printer and material manufacturers can also guide the selection of optimal parameter values [4].

✉ Ramona Dogea, ramona.dogea@strath.ac.uk | ¹Department of Design, Manufacture and Engineering Management (DMEM), University of Strathclyde, Glasgow, Scotland. ²National Manufacturing Institute Scotland (NMIS), University of Strathclyde, Glasgow, Scotland.



Relevant parameters are, amongst others, layer thickness, number of layers, infill, extruder temperature, printing bed temperature and printing speed [5].

FDM has been one of the most researched AM techniques due to its easy way of use and low-cost in the processing of thermoplastic polymers such as PLA, Acrylonitrile Butadiene Styrene (ABS), Nylon and Polyethylene Terephthalate (PET) [6]. Among them, PLA is commonly used for small-scaled prototypes, noting that it is a thermoplastic polyester that can be obtained from renewable resources. This material has higher strength and lower ductility compared to other traditional materials for rapid prototyping, such as Acrylonitrile Butadiene Styrene (ABS) [7]. Prototypes produced with PLA commonly use FDM [8]. As a result of its lower coefficient of thermal expansion, PLA has a lower deformation effect [9]. The basic mechanical properties of PLA are detailed in Table 1 [10, 11]. These mechanical properties correspond to the 3D printed parts and FEA analysis within this work.

In this work a case study was investigated involving an aircraft wing rib. Wing ribs are fundamental components of aircraft wings that perform specific functions. In addition the wing rib is the component that ultimately withstands wing torsion, doing this together with the skin and the spars [12]. Numerical techniques such as Finite Element Modelling (FEM) offer a sophisticated approach to characterising the strain of wing ribs and that were manufactured using PLA and subjected to complex loading conditions. FEM tools also allow verification of practical experiments when prototyping and testing [13].

Experiments can be conducted in different ways: trial and error, one-factor-at-a-time experiments, full-factorial experiments, and Taguchi's orthogonal arrays (OA). Taguchi's approach can eliminate the bias generated by one-factor-at-a-time experiments and helps improve the experimental performance of full-factorial experiments, it has been already applied to optimise parameters when fabricating polymeric parts with FFF [14] and to optimise properties for 3D printed PLA [15]. Furthermore the use of orthogonal arrays helps to reduce the time invested on experiments [16]. In this work Taguchi's procedure for the design of experiments (DoE) was used to study and analyse the effects of three variables, as described in the materials and methods section, on the deformation of a 3D-printed PLA aircraft wing rib. In this case, the $L_4(2^3)$ array was selected for the design of an experiment with three factors at two levels [17].

In the literature, experiments on PLA parts have shown that changes in the strain rate do not have a big influence on the linear region of the stress–strain curve. i.e., in the region of low stress levels [18, 19]. To evaluate material properties and structural performance of an aircraft wing, bending, torsion and traction tests are required. In current research, loads are often introduced on the ribs to reproduce wing root bending moment and shear, and torsional load are also included by adjusting the load position points [20].

Wing ribs are subjected to different loading conditions. Among them, bending, torsion and traction loading always occur on aircraft wings during flight [21]. When analysing wing rib performance, the traction loads on the lower skin of the wing box are also considered in order to model the inertial effect of the fuel weight in the wing [22]. In [23] it is stated that the maximum moment at the wing root results in pressured side plates with a traction effect on the wing. In addition engines and rotors mounted on the aircraft wing introduce traction and torsional effects on the wing box [24]. Wing ribs have been already tested and simulated to evaluate the effect of normal concentrated and distributed loads to emulate traction loads as well [13].

The main purpose of the work reported here has been to test and evaluate the strain under different loading conditions and testing set-ups in order to answer two research questions. The first one inquiries about the strain experienced by wing ribs with sensory capabilities under bending, torsion, and traction loads. The second one asks about the most significant factor that should be taken into account when testing wing ribs. When performing the experimental trials, some of the challenges associated with the evaluation of the structural performance of an aircraft wing rib made from PLA material using the FDM technique included:

Table 1 Mechanical properties of Polylactic Acid (PLA)

Parameter	Value
Density	1.24 g/cm ³
Young's modulus	3500 MPa
Poisson's ratio	0.36
Bulk modulus	5,167 MPa
Shear modulus	1287 MPa
Tensile yield strength	70 MPa
Tensile ultimate strength	73 MPa

- Variability in material properties: PLA material properties can vary due to differences in manufacturing processes, environmental factors, and other factors, which can affect the accuracy and consistency of test results.
- Limitations of FDM technique: the FDM technique used to print wing rib prototypes can lead to anisotropic material properties in the printed part, resulting in varying mechanical properties based on the direction of loading. Internal discontinuities formed during the FDM process can weaken the structural integrity of the part, potentially leading to premature failure or deformation. Due to these limitations, it is essential to consider them carefully when conducting structural performance tests and interpreting their results.
- Complexity of the wing rib geometry, which can make it difficult to accurately measure and interpret test results, especially in areas where stress concentrations occur.
- Limitations of testing equipment: the testing equipment used to perform the bending, torsion, and traction tests may have limitations in terms of accuracy, sensitivity, and resolution. This can affect the ability to accurately measure and interpret the results.

This research overcomes challenges associated with evaluating the structural performance of an aircraft wing rib made using PLA material and the FDM technique by subjecting a wing rib prototype to bending, torsion, and traction loading conditions, and identifying the linear region of material response for each test. This work contributes to knowledge by identifying factors affecting the performance of 3D-printed PLA wing ribs with IoT sensory capabilities and presenting an approach to evaluate the structural performance of such components using experimental testing and finite element analysis. This investigation involves both experimental testing and finite element analysis to assess the strain distribution in the structure under different loading conditions and testing set-ups. The Taguchi approach was used to identify the physical factors and interactions most relevant to this application. Results indicate that the bending load vs. strain curve is highly dependent on the applied load position and wing rib cut-out locations, and that the structural performance is also highly dependent on torsion. The use of sensory covers improves the component's ability to withstand traction load and reduces corresponding strain by up to 61%. The details are explained in the next sections.

2 Materials and methods

2.1 Model design

The wing rib was designed in Catia™ using the NACA 0018 profile. Cut-outs were introduced to reduce weight and to increase load resistance. In addition, cut-outs can be used to allow the wing interior equipment to pass through the ribs. The figure below shows the 3D model with a maximum length of 1000 mm, a maximum height of 180 mm and 3 mm web thickness with 6 mm upper and lower caps. To facilitate sensory integration that can allow collection of life cycle data the model was designed with three sensory locations and covers that can be assembled and disassembled for maintenance purposes. The dimensions of the wing rib and the sensory covers are shown in Figs. 1 and 2, respectively.

2.2 Fabrication of the wing rib prototype

The model was printed using FDM as the manufacturing technique based on PLA material, since it was for academic purposes and with the requirement for reducing testing costs.

2.3 STL files of wing rib and sensory cover

In order to print the 3D model the wing rib and the sensory cover were saved in Catia™ as.stl format files and imported to Ultimaker Cura™. To manufacture the wing rib a Discovery 3D printer was used. Considering its build volume there was the possibility of printing four identical parts in one job, Fig. 3. In the case of the sensory cover the CR-6 printer was used due to its reduced dimensions. Its build volume allowed the printing of 36 sensory covers in one job, Fig. 4.

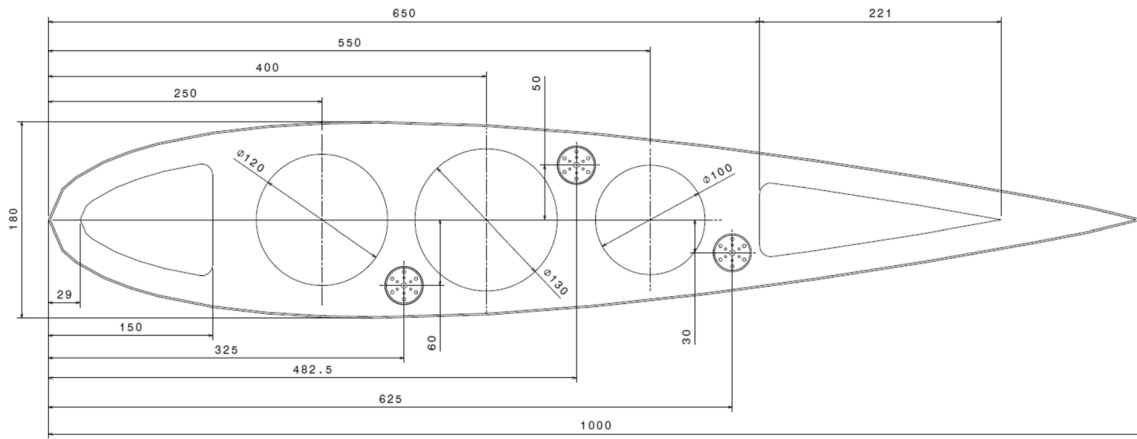


Fig. 1 Wing rib dimensions (mm)

Fig. 2 Sensory cover dimensions (mm)

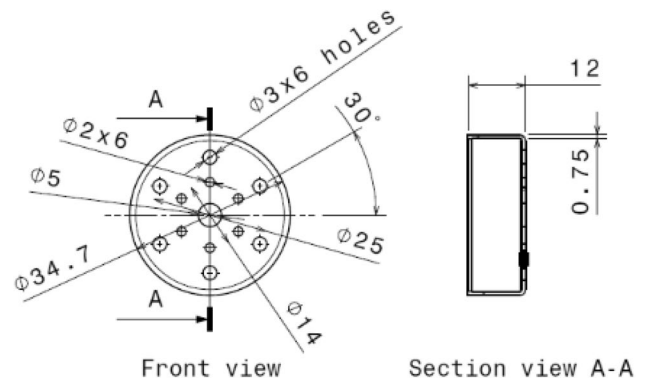


Fig. 3 Wing rib.stl file imported to Ultimaker Cura™

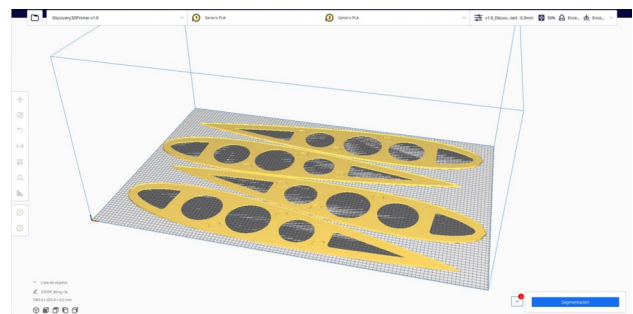


Fig. 4 Sensory cover.stl file imported to Ultimaker Cura™



2.4 3D printing

A Discovery 3D machine was used to get the wing rib prototype printed, Fig. 5, and a CR-6 machine to print the sensory covers, Fig. 6. The AM machines used for printing the prototype are described in Tables 2 and 3.

Fig. 5 Discovery 3D printer



Fig. 6 CR-6 printer

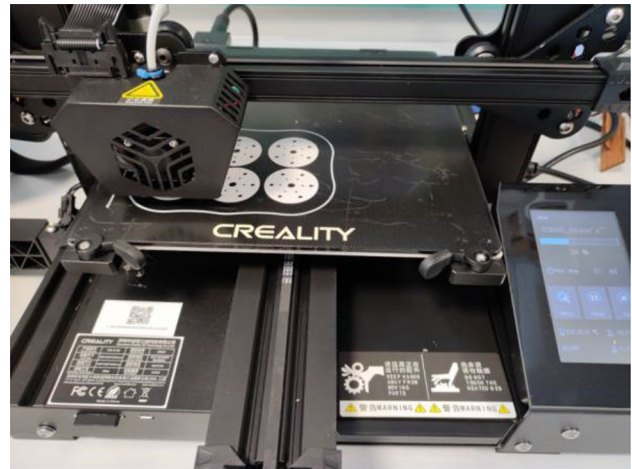


Table 2 Parameters of the Discovery printer

Description	Parameter
3D printer	Discovery 3D Printer
3D print build volume	1150 mm × 750 mm × 500 mm
Nozzle size	0.6 mm
Layer thickness	0.3 mm
Number of top and bottom layers	3
Infill	50%
Number of contours	3
Extruder temperature	235 °C
Printing bed temperature	70 °C
Printing speed	50 mm/s

Table 3 Parameters of the CR-6 printer

Description	Parameter
3D printer	CR-6 printer
3D print build volume	235 mm × 235 mm × 250 mm
Nozzle size	0.4 mm
Layer thickness	0.2 mm
Number of top and bottom layers	3
Infill	100%
Number of contours	3
Extruder temperature	215 °C
Printing bed temperature	60 °C
Printing speed	75 mm/s

Due to the rib length of 1000 mm a printing speed of 50 mm/s was selected in order to ensure optimal adhesion to the printing bed.

The Discovery Printer and the Ender Printer are two different models of 3D printers that utilize different mechanisms to achieve their printing capabilities. The Discovery Printer is a direct extrusion printer that operates with gear modules that are distinct from those used in the Ender Printer. Furthermore, the axes in the Discovery Printer are moved with servo motors rather than the stepper motors utilized in the Ender Printer. As a result, the Discovery Printer typically requires a slightly higher temperature to extrude materials and to achieve proper material deposition at the printer's operating speed. Additionally, the Discovery Printer features an aluminium bed that can be heated to promote improved adhesion and temperature distribution over the larger printing area. In contrast, the Ender Printer features a magnetic bed with a slightly roughened surface to enhance the adhesion of thermoplastics. This is a more effective method than the use of completely smooth metal beds. In addition, the printing speed of the machines was selected so that the parts could adhere well to the printing bed [25, 26].

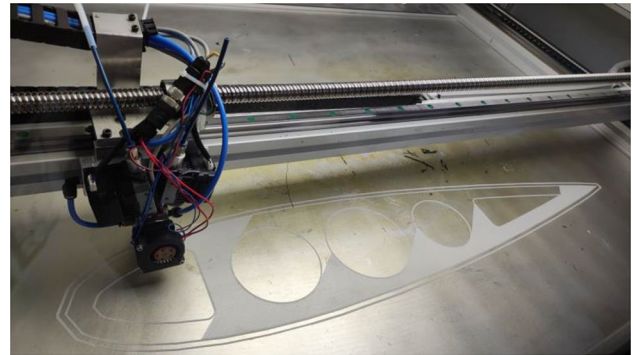
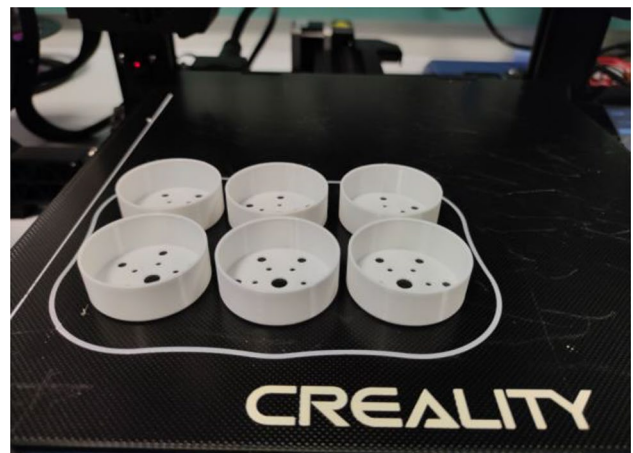
Fig. 7 3D printing of the wing wib**Fig. 8** 3D printing of the sensory covers

Table 4 Control parameters and levels

Control factor	Label	Level+	Level –
Bending load (N)	A	80	20
Load position (mm)	B	287	205
Crosshead speed (mm/min)	C	50	10

Fig. 9 Experimental set-up for the bending test

Figures 7 and 8, respectively, show one wing rib and six sensory covers being printed.

The infill of the PLA material was 90% for the wing rib and 100% for the sensory covers. The strength of PLA material can be influenced by the infill percentage used during the printing process. A higher infill percentage generally results in a stronger printed part due to increased structural support, which reduces the likelihood of deformation or cracking. However, higher infill percentages also come at the cost of increased printing time and material usage. It is important to note that other factors, such as layer height, print temperature, and cooling settings, can also have an impact on the strength of printed parts. Therefore, determining the optimal infill percentage for a specific application may require a comprehensive analysis of multiple factors, which may require experimentation to determine the best possible outcome [27–29].

2.5 Design of experiments (DoE)

In order to define the test procedure, the design of the experiments was based on Taguchi's $L_4 (2^3)$ array. The selected factors were chosen taking into consideration the possible variables that might be changed during the testing of the wing rib: the bending load, and the load position and crosshead speed of the testing equipment. The experiment involving these three factors was performed at two levels and the scope was to evaluate which factor can be shown to be dominant over the others. A summary of the control parameters and their levels is given by Table 4.

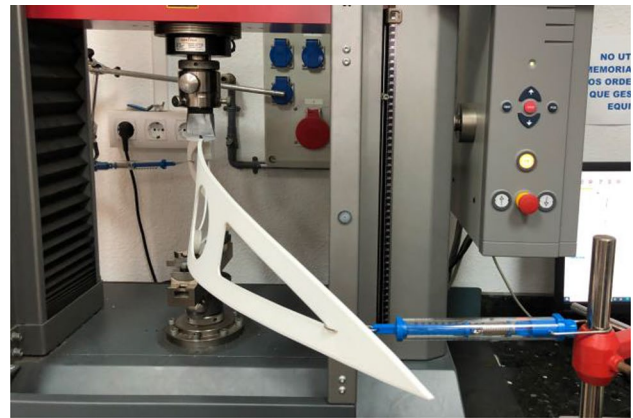
2.6 Experimental procedure

The 3D-printed PLA prototype was experimentally tested for bending, torsion and traction on a ProLine™ machine for standardised tests of the company ZwickRoell GmbH & Co. KG. Three set-ups were realised: a bending, a torsion and finally a traction tests. For the bending test a vertical load was applied for two different positions, defined respectively as D_1 and D_2 , at the upper cap, noting that the extremes of the leading and trailing edges were fixed in order to avoid flexing in the vertical plane. Figure 9 shows the set-up for the bending test.

When testing torsional effects on wing ribs it is complicated to perform the test as compared to one for a wing skin. This is due to the way the loading is applied to the wing structure and how different components within the structure support the loading. In a flight cycle during take-off the pressure increases under the aircraft wing and the pressure decreases above the wing structure. A small load on the top of the aerofoil and a larger load on the bottom of the aerofoil could be applied in different directions, i.e., horizontally and vertically.

In the torsion test, loads from different directions were applied by using dynamometers to achieve a torque or twisting motion (F_{dyn}). In addition to the bending load applied through the ProLine™ machine two perpendicular loads were

Fig. 10 Experimental set-up for the torsion test



used by using two dynamometers. In both the bending and torsion tests two crosshead speeds V_1 and V_2 were set. The torsion set-up is shown in Fig. 10.

Within the set-up the repeatability or level of measurable accuracy was reduced due to two factors. Firstly, as a result of the of the crosshead speed of the machine, the wing rib experimented flexing on its structure. Secondly, the supports used to fix the rib into the machine presented instability when applying the bending load.

The same ProLine™ machine was utilised to conduct a vertical traction test by changing the tools to generate the required load. The objective of this test was to evaluate the structural strength of the wing rib with and without the sensory covers and to compare their performance up to the point of failure. The test involved increasing the load incrementally by applying a single force in the plane of the wing rib. To ensure consistency and precision, the crosshead speed of the machine was set at a constant rate of $V_t = 20$ mm/min during the traction test. By performing this test, it was possible to measure and compare the mechanical properties of the wing rib with and without the sensory covers, providing valuable insight into their effect on the structural performance of the component. Figure 11 shows the set-up for the traction test.

Fig. 11 Experimental set-up for the traction test



Table 5 Summary of the parameters used during testing the wing rib

Parameters	Description	Value	Application scope
D_1 (mm)	Application point 1 of bending load (measured from the leading edge)	205	Bending and torsion
D_2 (mm)	Application point 2 of bending load (measured from the leading edge)	287	Bending and torsion
V_1 (mm/min)	Crosshead speed 1	10	Bending and torsion
V_2 (mm/min)	Crosshead speed 2	50	Bending and torsion
$F_{\text{dyn, le}}$ (N)	Applied force through dynamometer at the leading edge	- 6	Torsion
$F_{\text{dyn, te}}$ (N)	Applied force through dynamometer at the trailing edge	6	Torsion
V_t (mm/min)	Crosshead speed traction	20	Traction

Table 5 below summarises the parameters used for the above tests:

2.7 Finite element analysis

Ansys™ was used to simulate the testing conditions. The wing rib model was exported from CATIA® and meshed with tetrahedral elements. This tetrahedral element mesh was composed of 112,669 nodes and 55,172 elements, with an element size of 3.5 mm. The meshed wing rib with sensory covers is shown in Fig. 12.

Figures 13 and 14 show the boundary conditions used in the model considering the application load points at D_1 and D_2 . The position of the supports was also changed when the applied load points were changed.

The infill of the PLA material for the wing rib was defined by reducing the density by 10%, while for the sensory covers the density remained at 100%.

3 Results and discussion

3.1 Taguchi's experimental test layout

The Taguchi experimental test layout $L_4(2^3)$ in Table 4 was performed and the resulting strain was measured. The average strain value for the four runs was 0.004915 mm/mm. The results are shown in Table 6.

To check the influence of each control factor without considering any interactions between other factors, the averages of each level for each factor were calculated. The resulting main effect of each control factor was based on the difference between average levels. The highest effect belongs to factor A followed by factors B and C, Table 7. Thus, the most relevant factor in the experiments was seen to be the applied bending load (control factor A). This is displayed in the effects plot, Fig. 15. For each factor the vertical distance between the points is equal to the size of the effect of this factor.

In order to check the interactions between the control factors a graphical representation of the interactions between factors can be constructed. The levels of one factor are represented on the horizontal axis, while the levels of the other factor are indicated by two lines. If the lines are parallel to each other, there is no interaction between the two factors, but if the lines are not parallel to each other, then there is an interaction between the two factors. Between factors A

Fig. 12 Mesh generation in Ansys™

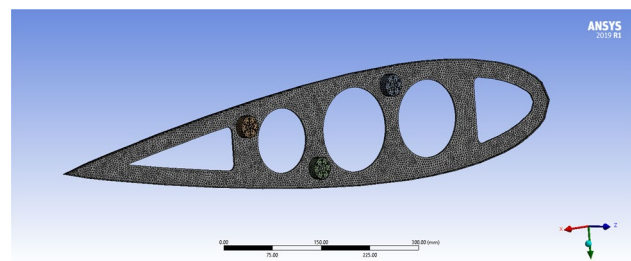


Fig. 13 Ansys™ model with bending load at D_1

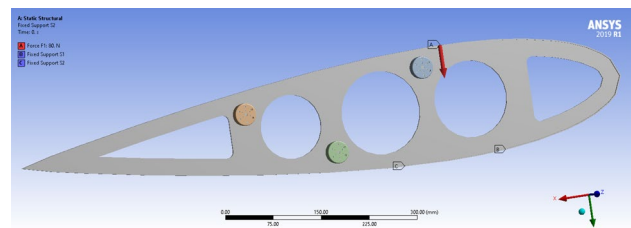


Fig. 14 Ansys™ model with bending load at D_2

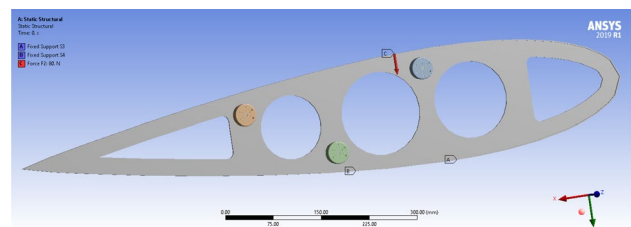
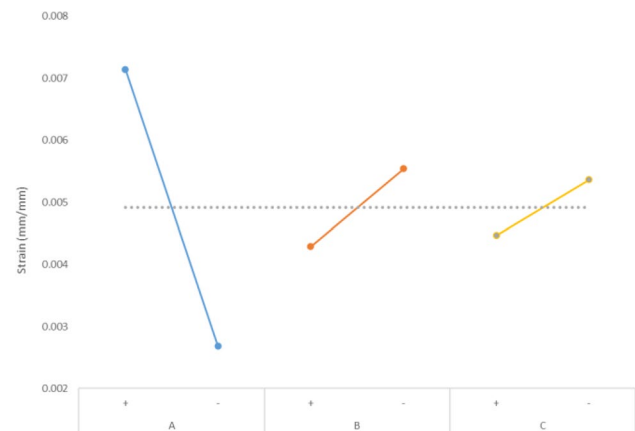


Table 6 Taguchi's experimental test layout L_4 (2^3) array

Run	L_4 OA—inner array (control factors)			L_1 OA—outer array (response) Strain (mm/mm)
	A	B	C	
1	+	+	+	0.006070
2	+	−	−	0.008217
3	−	+	−	0.002511
4	−	−	+	0.002860
	Average value			0.004915

Table 7 Response table

Control factors	A	B	C
Level average +	0.007144	0.004291	0.004465
Level average −	0.002686	0.005539	0.005364
Main effect	0.004458	0.001248	0.000899

Fig. 15 Main effects plot

and B there is no interaction since the lines are almost parallel to each other. In case of the interaction between A and C, the segments are not parallel and they are seen to cross, so there is an interaction between them. This also happens to factors B and C. The interactions plots are shown in Fig. 16.

3.2 Bending test

The next step was to vary experimentally the bending load to obtain the corresponding strain. The linear region of the bending load versus equivalent elastic strain was obtained by varying the bending load up to around 100 N, while the nonlinear region of the curve was obtained by loading the rib up to around 190 N. The target of obtaining the non-linear region was to determine the maximum load that the wing rib can withstand. Simulations were performed in Ansys™ examining the linear region since the use of nonlinear models for PLA was not within the scope of this work. Thus, the work has been necessarily constrained to the linear stress–strain region for the material, and the purpose of testing the prototype was to verify its structural behaviour under the application of bending, torsion and traction loads.

Figure 17 shows the linear region of the wing rib with sensory covers (SC) for D_1 , D_2 , V_1 and V_2 . In addition, the simulation of this linear region was undertaken in Ansys™ to validate the experiments. Since the crosshead speed was less relevant than the bending load and the application load point, its effect was not considered in the simulations.

In the images below the equivalent elastic strain is displayed for an 80 N bending load applied at D_1 (Fig. 18) and D_2 (Fig. 19), where the points of maximum strain can be found for both cases, respectively:

A summary of the experiments and simulations considering a bending load of 80 N are shown in Table 8. The error between the FEA and the experimental results is 0.51% for the case D_2 and V_1 , whilst the other cases present an error between 18 and 27%. The points taken to measure the strain obtained through the simulations were D_1 and D_2 . The error

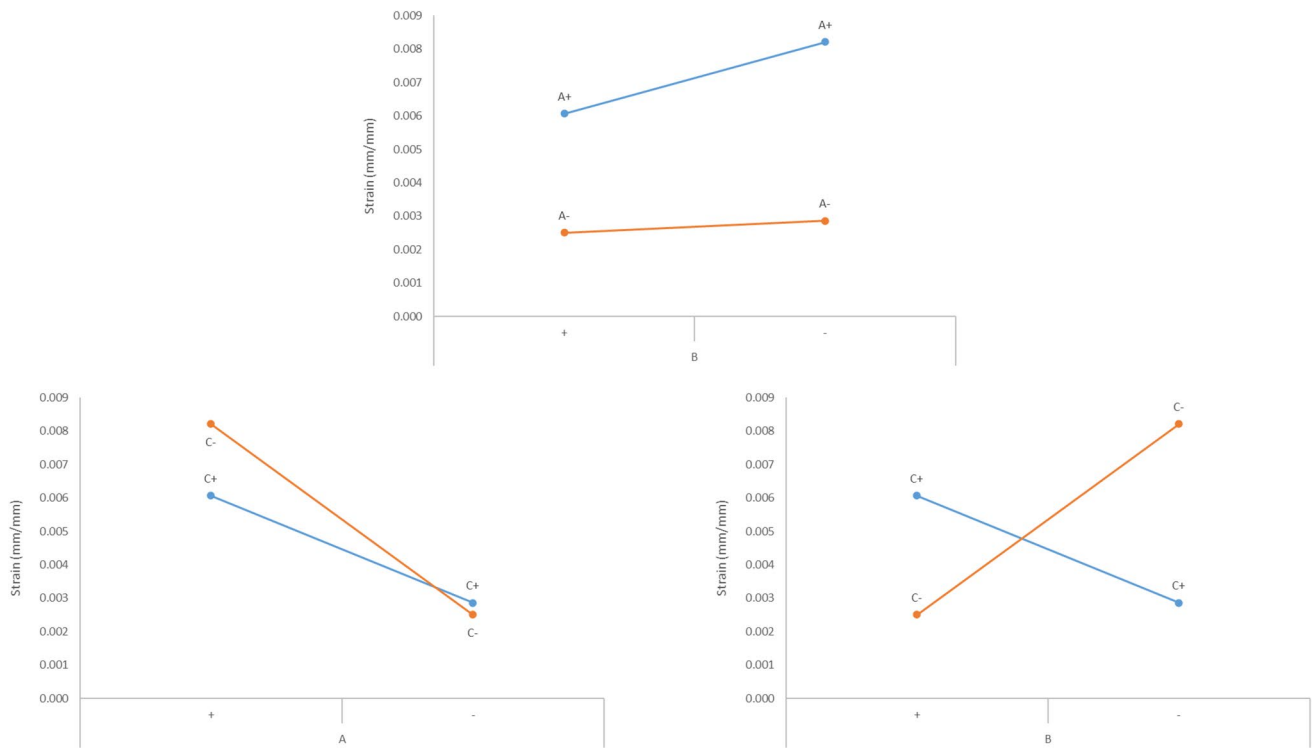


Fig. 16 Interaction plots between control factors

Fig. 17 Comparison of experimental results and simulations of bending force versus equivalent elastic strain

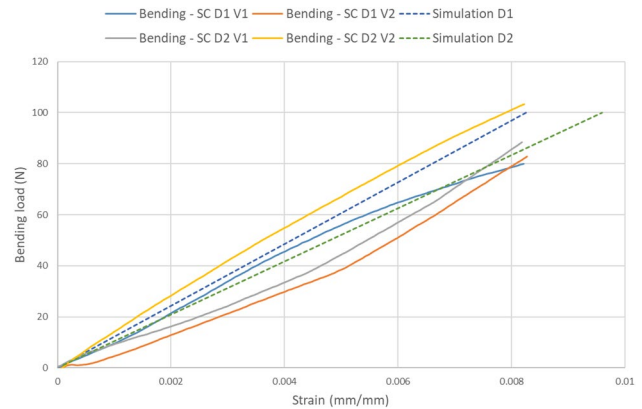
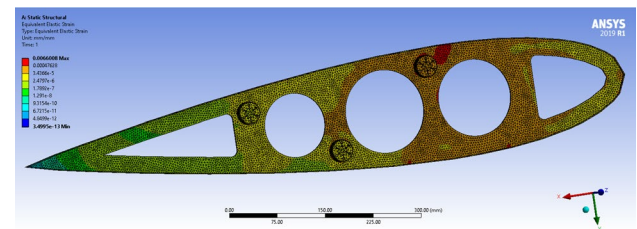


Fig. 18 Simulation results with an 80 N bending load at D_1



between experimental trials and simulations occurred as a result of the experimental set-up. Due to the sensitivity while applying boundary conditions during the trials the accuracy of the results was affected.

During the experimental trials the bending load was varied from 80 N up to around 190 N to examine the nonlinear region of the bending force versus equivalent elastic strain. When the load was applied at D_1 , the wing rib showed that it could better withstand behaviour for V_2 than V_1 . The opposite occurred when the load was applied at D_2 and it could

Fig. 19 Simulation results with an 80 N bending load at D_2

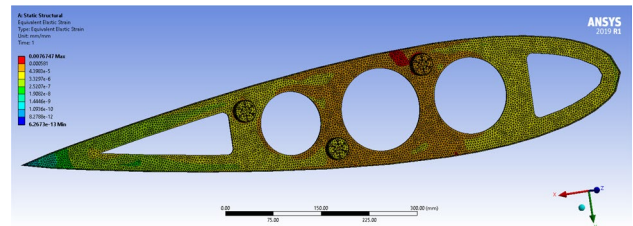


Table 8 Comparison of experiments and simulations of the linear region for a bending load of 80 N

Bending load application point	D_1		D_2	
	V_1	V_2	V_1	V_2
Strain—FEA result (mm/mm)	0.006601	0.006601	0.007675	0.007675
Strain—Experimental result (mm/mm)	0.008217	0.008078	0.007636	0.006070
Error (%)	19.67	18.29	0.51	26.44

Fig. 20 Experimental results for bending load versus strain

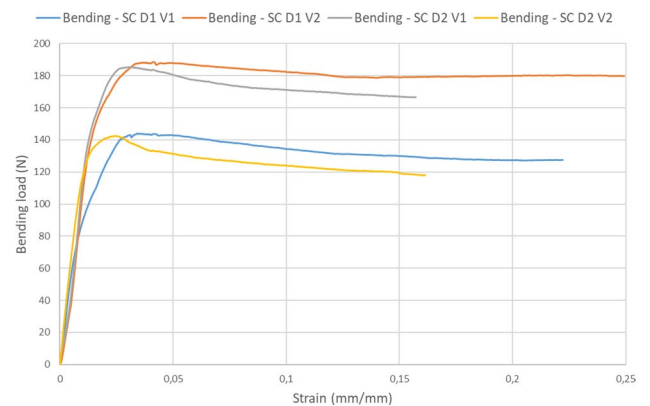
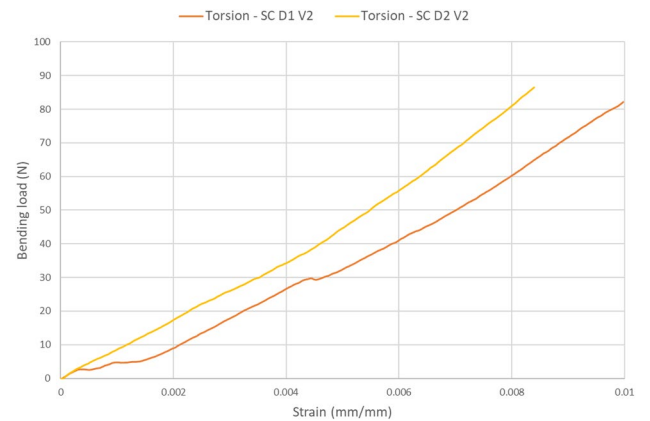


Fig. 21 Experimental results of torsion test



better withstand behaviour for V_1 (Fig. 20). This is explained because of the wing rib geometry whereby the structural performance is seen to depend highly on the applied load position. The location of the cut-outs also has considerably influence on the material strain.

3.3 Torsion test

In order to verify a twisting motion, a torsion test was also performed to check strain variations. The tests were done at the location points D_1 and D_2 with speed V_2 and by using two dynamometers. The linear region is shown in Fig. 21.

To verify the results a load of 2 N located on the top of the aerofoil was simulated besides the forces $F_{dyn, le}$ and $F_{dyn, te}$. The points to measure the strain obtained by means of the simulations were at D_1 and D_2 . The results are shown in Table 9. In the case of the torsion test, the difficulty consisted of applying the loads using the dynamometers and maintaining the wing rib stability when employing the bending load.

Table 9 shows the error presented between the measurements and the simulations, up to 29%. In torsion testing of parts made of PLA, there can be several sources of error in the strain measurement that can cause differences between FEA simulation and experimental results. During these trials, some possible sources of error were identified: (a) the material properties of PLA used in the simulation may not exactly match the material properties of the actual material used in the experiment, which leads to differences in the measured strain; (b) the fixture used to hold the specimen during the torsion test can also introduce errors in the strain measurement since they can introduce bending moments and shear forces that may not be accounted for in the simulation; (c) the friction between the specimen and the grips of the testing machine can cause deformation of the specimen and lead to errors in the strain measurement; (d) The technique used to measure the strain can also cause errors. For example, the machine tools and the dynamometers may not be placed accurately.

The images in Figs. 22 and 23 show the equivalent strain results and the deformed wing rib in the XZ-plane in the simulations:

3.4 Traction test

A traction test was performed to compare the failure load of the wing rib both with and without the sensory covers, defined as SC and NC respectively. The first traction NC test was performed by positioning the machine tool at the upper cap of the wing rib. The cap failed at a load of around 1202 N with a strain of 3.28 mm/mm, and this is defined as failure 1.

The second traction NC test was performed by positioning the machine tool at the surface of the wing rib plane. The prototype presented 3 structural failures during this test. The first failure occurred on one PLA filament of the wing rib upper cap (defined as failure 2) at a load of 1686 N and a strain of 3.44 mm/mm. The second failure took place between a cut-out and an upper cap (defined as failure 3) at a load of 1762 N and a strain of 4.36 mm/mm. The structural damage of this failure did not stop the rib from operating in service, and it was still possible to increment further the traction load. Finally the prototype failed at a load of 749 N and a strain of 5.59 mm/mm (defined as failure 4) between two cut-outs.

Table 9 Comparison of experiments and simulations of the linear region for a bending load of 2 N

Crosshead speed	V_2	
Bending load application point	D_1	D_2
Strain—FEA result (mm/mm)	0.000279	0.000268
Strain—Experimental result (mm/mm)	0.000245	0.000207
Error (%)	13.85	29.20

Fig. 22 Simulation results with a 2 N bending load at D_1



Fig. 23 Simulation results with a 2 N bending load at D_2



Fig. 24 Traction test

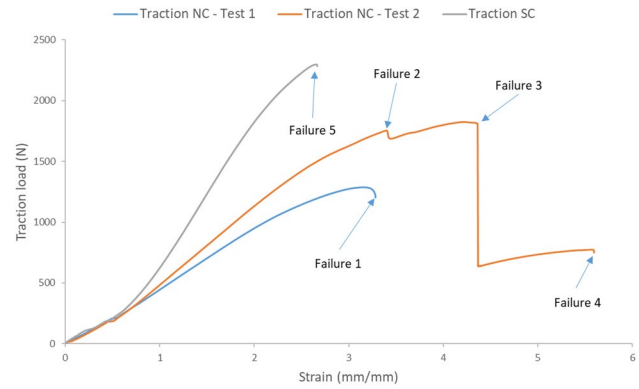


Table 10 Summary of the results for the traction tests

Test	Failure number	Failure load (N)	Failure strain (mm/mm)	Failure location
Traction NC—Test 1	1	1201.56	3.28	Wing rib upper cap
Traction NC—Test 2	2	1686.13	3.44	PLA filament at wing rib upper cap
	3	1762.26	4.36	Between cut-out and upper cap
	4	749.60	5.59	Between cut-outs
Traction SC	5	2283.05	2.66	Between cut-out and upper cap

The traction SC test was achieved by positioning the tool at exactly the same position measured for the second traction NC test. The failure occurred at 2283 N and a strain of 2.66 mm (defined as failure 5) between a cut-out and an upper cap. The results of these tests are shown in Fig. 24.

The tests and their results as well as the failure locations are summarised in Table 10.

Table 11 gives a visual overview of each failure and its location area:

The rate between the loads and strains of the NC and SC traction tests may be determined using the values of loads and strains for failures 3 and 5:

$$Failure\ load\ rate = \frac{Failure\ load_{SC}}{Failure\ load_{NC}} = \frac{2283.05\ N}{1762.26\ N} = 1.296$$

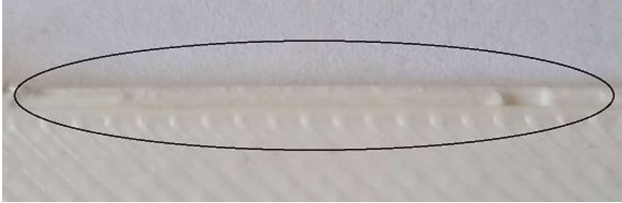
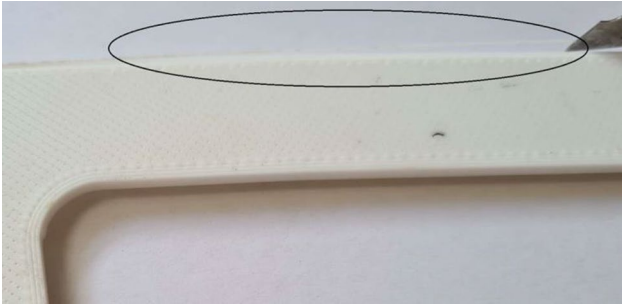
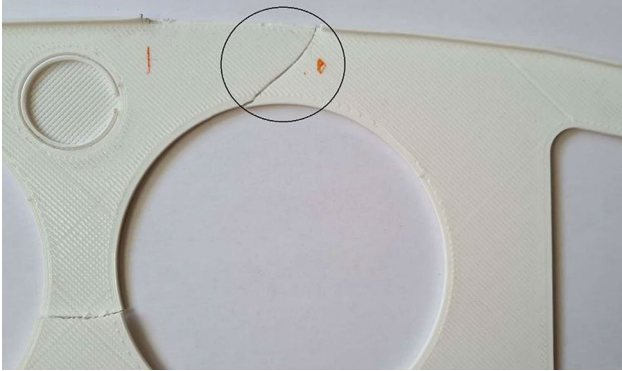


$$Failure\ strain\ rate = \frac{Failure\ strain_{SC}}{Failure\ strain_{NC}} = \frac{2.66\ mm/mm}{4.36\ mm/mm} = 0.610$$

The wing rib with the sensory covers can withstand a 29.6% higher load and presents 61% less strain at the failure point in the traction test.

4 Conclusions and future work

This study aimed to evaluate the structural performance of an aircraft wing rib made using PLA material and the FDM technique. To achieve this objective, a wing rib prototype was subjected to bending, torsion, and traction loading conditions to assess the structural performance of such components using experimental testing and finite element analysis. By identifying the factors affecting the performance of 3D-printed PLA wing ribs with IoT sensory capabilities, this research contributes to knowledge in the field. Furthermore, the linear region of material response for each test was determined. In order to evaluate the strain distribution in the structure under different loading conditions and testing set-ups, both experimental testing and finite element analysis were performed. The Taguchi approach was employed to identify the physical factors and interactions that are most relevant to this application. Results indicate that the bending load vs. strain curve is highly dependent on the applied load position and wing rib cut-out locations, and that the structural performance is also highly dependent on torsion. The use of sensory covers was found to significantly improve the

Table 11 Overview of wing rib failures and their position

Failure number	Caption	Cause of failure
1		Fracture
2		PLA filament damage
3		Fracture
4		Fracture
5		Fracture

component's ability to withstand traction load and reduce the corresponding strain by up to 61%. The study also showed that the bending load-strain curve depends highly on the applied load position and the wing rib cut-out locations. The linear region of the PLA material ranges up to around a bending load of 100 N and an equivalent strain of 0.008 mm/mm. The structural performance of the wing rib was also found to be highly dependent on the twisting motion. In the torsion tests, the linear region of the curve bending load-strain was found between 0 N and around 80 N, and equivalent strain between 0 mm/mm and around 0.008 mm/mm. Finally, the study also investigated the factors that are most relevant when performing bending tests. It was determined that the most relevant factor was the applied load and the interactions between the load location and the crosshead speed of the testing machine. Overall, the findings of this study provide valuable insights into the structural performance of 3D-printed PLA wing ribs and highlight the importance of considering different loading conditions and testing set-ups in order to accurately evaluate their performance.

Further work will be concentrated on the integration of smart devices into the wing rib structure and the implementation of IoT sensors. The purpose of this is to gather life cycle data which can be used to transition from a condition-based preventive maintenance system to a predictive maintenance-based system driven by data.

Acknowledgements The authors acknowledge the support of the University of Strathclyde (Scotland, United Kingdom), the Universidad Politécnica de Cartagena (Cartagena, Spain) and the Centro de Referencia Nacional de Formación Profesional Química (Cartagena, Spain) for using their facilities and equipment.

Author contributions RD wrote the original draft preparation. All authors reviewed the manuscript. All authors read and approved the final manuscript.

Funding This research was supported by the University of Strathclyde (Glasgow, Scotland).

Data availability All data generated or analysed during this study are included in this published article.

Code availability The code is available by request.

Declarations

Ethics approval and consent to participate Not applicable.

Competing interests The authors declare no competing interests.

Open Access This article is licensed under a Creative Commons Attribution 4.0 International License, which permits use, sharing, adaptation, distribution and reproduction in any medium or format, as long as you give appropriate credit to the original author(s) and the source, provide a link to the Creative Commons licence, and indicate if changes were made. The images or other third party material in this article are included in the article's Creative Commons licence, unless indicated otherwise in a credit line to the material. If material is not included in the article's Creative Commons licence and your intended use is not permitted by statutory regulation or exceeds the permitted use, you will need to obtain permission directly from the copyright holder. To view a copy of this licence, visit <http://creativecommons.org/licenses/by/4.0/>.

References

1. Bardot M, Schulz MD. Biodegradable poly(Lactic acid) nanocomposites for fused deposition modeling 3d printing. *Nanomaterials*. 2020. <https://doi.org/10.3390/nano10122567>.
2. Divyathej MV, Varun M, Rajeev P. Analysis of mechanical behavior of 3D printed ABS parts by experiments. *Int J Sci Eng Res*. 2016; 7(3).
3. Mushtaq RT, Iqbal A, Wang Y, Cheok Q, Abbas S. Parametric effects of fused filament fabrication approach on surface roughness of acrylonitrile butadiene styrene and nylon-6 polymer. *Materials*. 2022. <https://doi.org/10.3390/ma15155206>.
4. Kichloo AF, Aziz R, Haq MIU, Raina A. Mechanical and physical behaviour of 3D printed polymer nanocomposites—a review. *Int J Ind Syst Eng*. 2021. <https://doi.org/10.1504/IJISE.2021.116929>.
5. Kechagias J, Chaidas D. Fused filament fabrication parameter adjustments for sustainable 3D printing. *Mater Manuf Processes*. 2023. <https://doi.org/10.1080/10426914.2023.2176872>.
6. Mohan N, Senthil P, Vinodh S, Jayanth N. A review on composite materials and process parameters optimisation for the fused deposition modelling process. *Virtual Phys Prototyping*. 2017. <https://doi.org/10.1080/17452759.2016.1274490>.
7. Fehri S, Cinelli P, Coltelli M-B, Anguillesi I, Lazzeri A. Thermal properties of plasticized poly (Lactic Acid) (PLA) containing nucleating agent. *Int J Chem Eng Appl*. 2016;7(2):85–8. <https://doi.org/10.7763/ijcea.2016.v7.548>.
8. Torres J, Cole M, Owji A, DeMastry Z, Gordon AP. An approach for mechanical property optimization of fused deposition modeling with polylactic acid via design of experiments. *Rapid Prototyping J*. 2016. <https://doi.org/10.1108/RPJ-07-2014-0083>.
9. Letcher T. Material property testing of 3d-printed specimen in PLA on an entry-level 3d printer. *Proceedings of the ASME 2014 International Mechanical Engineering Congress and Exposition*, 2016.

10. Jayakumar N, Senthilkumar G, Pradeep AD. Effect of printing parameters of 3D printed PLA parts on mechanical properties. *J Eng Res (Kuwait)*. 2021. <https://doi.org/10.36909/jer.ICMMM.15697>.
11. Anand Kumar A, Shivraj Narayan Y. Tensile testing and evaluation of 3D-printed PLA specimens as per ASTM D638 type IV standard. in *Lecture Notes in Mechanical Engineering*, 2019. https://doi.org/10.1007/978-981-13-2718-6_9.
12. Bennaceur MA, Xu Y, Layachi H. Wing rib stress analysis and design optimization using constrained natural element method. *IOP Conf Ser Mater Sci Eng*. 2017;234(1):12018. <https://doi.org/10.1088/1757-899X/234/1/012018>.
13. Carneiro PMC, Gamboa P. Structural analysis of wing ribs obtained by additive manufacturing. *Rapid Prototyping J*. 2019;25(4):708–20. <https://doi.org/10.1108/RPJ-02-2018-0044>.
14. Kechagias JD, Zaoutsos SP. Optimising fused filament fabrication surface roughness for a dental implant. *Mater Manuf Processes*. 2023. <https://doi.org/10.1080/10426914.2023.2176870>.
15. Kafshgar AR, Rostami S, Aliha MRM, Berto F. Optimization of properties for 3D printed PLA material using Taguchi, ANOVA and multi-objective methodologies. *Procedia Struct Integr*. 2021. <https://doi.org/10.1016/j.prostr.2021.12.011>.
16. Prabhu R, Ganapathy T, Venkatachalapathy VSK. Process parameters optimization on porthole-die hot extrusion of aluminium alloy tubes using Taguchi method. *Int J Mech Mater Eng*. 2011;6(1).
17. Freddi A, Salmon M. Introduction to the Taguchi Method. In *Springer Tracts in Mechanical Engineering*, 2019, pp. 159–180. https://doi.org/10.1007/978-3-319-95342-7_7.
18. Ji Q, Wang Z, Yi J, Tang X. Mechanical properties and a constitutive model of 3d-printed copper powder-filled pla material. *Polymers*. 2021. <https://doi.org/10.3390/polym13203605>.
19. Sweeney J, Spencer P, Nair K, Coates P. Modelling the mechanical and strain recovery behaviour of partially crystalline PLA. *Polymers*. 2019. <https://doi.org/10.3390/polym11081342>.
20. Schneider J, Frangenberg M, Notter S, Scholz W, Fichter W, Strohmayer A. Integration of propelled yaw control on wing tips: a practical approach to the Icaré solar-powered glider. *CEAS Aeronaut J*. 2022. <https://doi.org/10.1007/s13272-022-00603-4>.
21. Bin Mohd Zakuan MAM, Aabid A, Khan SA. Modelling and structural analysis of three-dimensional wing. *Int J Eng Adv Technol*. 2019;9(1):6820–8. <https://doi.org/10.35940/ijeat.A2983.109119>.
22. Brooks TR, Kennedy G, Martins JRRR. High-fidelity Multipoint Aerostructural Optimization of a High Aspect Ratio Tow-steered Composite Wing. in *58th AIAA/ASCE/AHS/ASC Structures, Structural Dynamics, and Materials Conference*, Reston, Virginia: American Institute of Aeronautics and Astronautics, 2017. <https://doi.org/10.2514/6.2017-1350>.
23. Groth C, et al. Structural validation of a realistic wing structure: the RIBES test article. *Procedia Struct Integr*. 2018;12:448–56. <https://doi.org/10.1016/j.prostr.2018.11.073>.
24. De Oliveira BA. Wing structural optimization for electric distributed propulsion aircraft using genetic algorithm wing structural optimization for electric distributed propulsion aircraft using genetic algorithm. 2020.
25. Bárcenas C. *Discovery 3D Printer*. Technical specifications. 2021. [Online]. Available: <https://discovery3dprinter.com/catalogos/eng/Discovery3DPrinterENG.pdf>.
26. S. C. 3D Technology, “CR-6 SE. 3D Printer User Manuel.” 2020.
27. Abeykoon C, Sri-Amphorn P, Fernando A. Optimization of fused deposition modeling parameters for improved PLA and ABS 3D printed structures. *Int J Lightweight Mater Manuf*. 2020. <https://doi.org/10.1016/j.ijlmm.2020.03.003>.
28. Verbeeten WMH, Lorenzo-Bañuelos M. Material extrusion additive manufacturing of Poly(Lactic Acid): influence of infill orientation angle. *Addit Manuf*. 2022. <https://doi.org/10.1016/j.addma.2022.103079>.
29. Ezeh OH, Susmel L. On the fatigue strength of 3D-printed polylactide (PLA). *Procedia Struct Integr*. 2018. <https://doi.org/10.1016/j.prostr.2018.06.007>.

Publisher's Note Springer Nature remains neutral with regard to jurisdictional claims in published maps and institutional affiliations.